Kinematics and physical properties of southern interacting galaxies: the minor merger AM 2306–721

A. C. Krabbe,[1,2]⋆ M. G. Pastoriza,[1] Cláudia Winge,[3] I. Rodrigues[4] and D. L. Ferreiro[5]

[1]*Instituto de Física, Universidade Federal do Rio Grande do Sul, Av. Bento Gonçalves 9500, Cep 91359-050, Porto Alegre, RS, Brazil*
[2]*Southern Astrophysical Research Telescope, c/o AURA Inc., Casilla 603, La Serena, Chile*
[3]*Gemini Observatory, c/o AURA Inc., Casilla 603, La Serena, Chile*
[4]*Universidade do Vale do Paraíba, Av. Shishima Hifumi 2911, Cep 12244-000, São José dos Campos, SP, Brazil*
[5]*IATE, Observatório Astronómico, Universidad Nacional de Córdoba, Laprida 854, 5000 Córdoba, Argentina*

ABSTRACT

We present an observational study about the effects of the interactions in the kinematics, stellar population and abundances of the components of the galaxy pair AM 2306-721. Rotation curves for the main and companion galaxies were obtained, showing a deprojected velocity amplitude of 175 and 185 km s^{-1}, respectively. The interaction between the main and companion galaxies was modelled using numerical *N*-body/hydrodynamical simulations, with the result indicating that the current stage of the merger would be about 250 Myr after perigalacticum. The spatial variation in the distribution of the stellar-population components in both galaxies was analysed by fitting combinations of stellar-population models of different age groups. The central region of main galaxy is dominated by an old (5–10 Gyr) population, while significant contributions from a young (200 Myr) and intermediate (1 Gyr) components are found in the disc, and being enhanced in the direction of the tidal features. The stellar population of the companion galaxy is overall much younger, being dominated by components with 1 Gyr or less, quite widely spread over the whole disc. Spatial profiles of the oxygen abundance were obtained from a grid of photoionization models using the R_{23} line ratio. The disc of the main galaxy shows a clear radial gradient, while the companion galaxy presents oxygen abundance relatively homogeneous across the disc. The absence of an abundance gradient in the secondary galaxy is interpreted in terms of mixing by gas flows from the outer parts to the centre of the galaxy due to the gravitational interaction with the more massive primary.

Key words: galaxies: abundances – galaxies: general – galaxies: interactions – galaxies: kinematics and dynamics – galaxies: starburst – galaxies: stellar content.

1 INTRODUCTION

It is widely accepted by some time that merging and interaction events play an important role in the formation and evolution of galaxies. Mergers change the mass function of galaxies, creating a progression from small galaxies to larger ones; the merging process can also change the morphology of the constituents, transforming gas-rich spirals in quiescent ellipticals. Interactions can also trigger a wide set of physical and morphological phenomena, such as tidal tails, bridges and shells, kinematically decoupled cores and star-formation enhancements (see review of Struck 1999).

Interacting galaxies also show enhanced star formation when compared with isolated galaxies. Such enhancement was initially proposed by Larson & Tinsley (1978) to explain the wider range of optical colours found in galaxies in pairs. Since then, numerous studies have confirmed these results, especially in the central regions, through measurements of optical emission lines (Kennicutt & Keel 1984; Kennicutt et al. 1987; Donzelli & Pastoriza 1997; Barton Gillespie, Geller & Kenyon 2003; Woods & Geller 2007), infrared emission (Joseph & Wright 1985; Sekiguchi & Wolstencroft 1992; Geller et al. 2006) and radio emission (Hummel 1981). Recent studies have also shown that this enhancement is a function of the projected galaxy pair separation (e.g. Barton, Geller & Kenyon 2000; Lambas et al. 2003; Nikolic, Cullen & Alexander 2004), being stronger in low mass than in high-mass galaxies (e.g. Woods & Geller 2007; Ellison et al. 2008). In particular, Ellison et al. (2008) found that the star-formation rate as measured by the Hα equivalent width for galaxies in pairs selected from the Sloan Digital Sky Survey, is some 70 per cent higher when compared to a control sample of galaxies with equal stellar mass distribution.

⋆E-mail: angela.krabbe@ufrgs.br

There is a connection between the interaction strength and the morphological distortion in binary galaxies. According to Mihos & Hernquist (1996) models, the response of the gas to a close passage depends dramatically on the mass distribution of the galaxy, with the irregularities in the gas velocity field tracing the disturbances in the gravitational potential of the galaxy as observed, for example, in some galaxies in the Virgo cluster (Rubin, Waterman & Kenney 1999). Combined *N*-body/hydrodynamic simulations show that galaxy–galaxy mergers disturb the gas velocity field significantly, and hence lead to asymmetries and distortions in the rotation curves (Kronberger et al. 2006). However, according to these authors, no severe distortions are observable about 1 Gyr after the first encounter.

The gas motions created by the interaction can also significantly alter the chemical state of the galaxies (Koeppen & Arimoto 1990; Dalcanton 2007), and modify the usually smooth radial metallicity gradient often found in isolated disc galaxies (Henry & Worthey 1999). Recently, Kewley, Geller & Barton (2006) found that O/H abundance in the central region of nearby galaxy pairs is systematically lower than that of isolated objects. These authors suggest that the lower metallicity is a consequence of gas infall caused by the interaction, but very few observational studies have been published analysing in detail the influence of different levels of interactions in the metallicity distribution and enrichment properties of galaxies.

Ferreiro & Pastoriza (2004) (hereafter FP04), in a study of the integrated photometry and star-formation activity in a sample of interacting systems from the Arp-Madore catalogue (Arp & Madore 1987), found that the galaxies involved have bluer colours than those of isolated galaxies of the same morphological type, indicating an enhancement of star-forming activity. This enhancement was also previously suggested by Donzelli & Pastoriza (1997) to explain the slightly larger values of Hα + N II equivalent widths found in these systems, when compared with normal isolated spiral galaxies. From their sample, we have selected several systems to start a more comprehensive study of the effects of the interactions in the kinematics, stellar population and abundances of the galaxies in the so-called 'minor merger' systems, defined here as physical pairs with mass ratio in the range of $0.04 < M_{secondary}/M_{primary} < 0.2$.

This paper presents the results for the system AM 2306-721. This pair is composed by a peculiar spiral with disturbed arms (hereafter, AM 2306A) in interaction with an irregular galaxy (hereafter, AM 2306B). Both galaxies contain very luminous H II regions with Hα luminosity in the range of $8.30 \times 10^{39} < L(H\alpha) < 1.27 \times 10^{42}$ erg s^{-1} as estimated from Hα images (Ferreiro, Pastoriza & Rickes 2008); and high star-formation rate in the range of 0.07–10 M yr^{-1} (Ferreiro et al. 2008). The present paper is organized as follows: in Section 2, we summarize the observations and data reduction. Section 3 describes the gas kinematics of each galaxy, and Section 4 presents the numerical *N*-body/hydrodynamical simulations of the interaction. Section 5 presents the stellar-population synthesis. The metallicity analysis is presented in Section 6, and the conclusions are summarized in Section 7.

2 OBSERVATIONS AND DATA REDUCTION

Long slit spectroscopic data were obtained in 2006 June 20/21 and 2007 June 23/24 with the Gemini Multi-Object Spectrograph at Gemini South (GMOS-S), as part of poor weather programmes GS-2006A-DD-6 and GS-2007A-Q-76. Spectra in the range 3350–7130 Å were taken in two settings with the B600 grating, and the 1 arcsec slit, yielding a spectral resolution of 5.5 Å. The frames were binned on-chip by 4 and 2 pixels in the spatial and spectra directions,
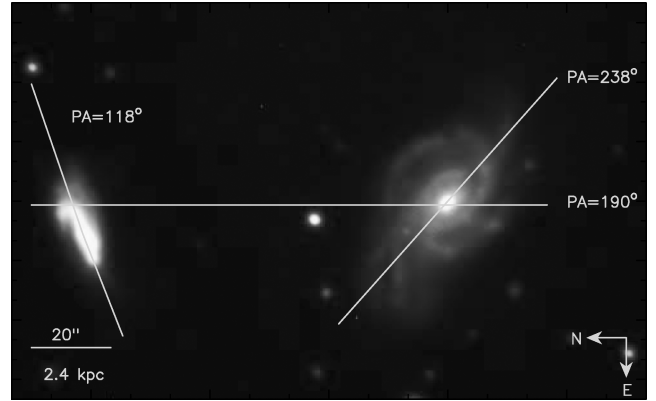

Figure 1. GMOS-S *r'*-band image of AM 2306-721 with the observed slit positions.

respectively, resulting in a spatial scale of 0.288 arcsec pixel^{-1}, and 0.9 Å pixel^{-1} dispersion.

Spectra were taken at three different position angles on the sky: PA $= 238°$ and $118°$ corresponding to positions along the major axis of AM 2306A and AM 2306B, respectively; and PA $= 190°$, a position cutting across the disc of both galaxies. The exposure time on each single frame was limited to 700 s to minimize the effects of cosmic rays, with four frames being obtained for each slit position to achieve suitable signal. The slit positions are shown in Fig. 1, superimposed on the *r'*-band image of the pair. Table 1 gives the journal of observations. Conditions during both runs were not photometric, with thin cirrus and image quality in the range 1.0–2.5 arcsec (as measured from stars in the acquisition images taken just prior to the spectroscopic observations).

The spectroscopic data reduction was carried out using the GEMINI.GMOS package as well as generic IRAF tasks. We followed the standard procedure for bias correction, flat fielding, cosmic ray cleaning, sky subtraction, wavelength and relative flux calibrations. In order to increase the signal-to-noise ratio, the spectra were then extracted summing over six rows. Each spectrum thus represents an aperture of 1×1.73 arcsec^2. For a distance of 119 Mpc for AM 2306A and 116 Mpc for AM 2306B (estimated from the radial velocities derived in Section 3 and adopting $H_0 = 75$ km s^{-1} Mpc^{-1}), this aperture corresponds to a region of 577×998 pc^2 for AM 2306A; and 562×972 pc^2 for AM 2306B. The nominal centre of each slit was chosen to be the continuum peak at $\lambda 5525$ Å. Figs 2 and 3 show a sample of spectra of AM 2306A and AM 2306B extracted along the slit for PA $= 238°$ and $118°$, respectively. Fig. 4 shows the Hα image of AM 2036B and AM 2036A. Description and detailed analysis of these images were presented in FP04.

3 IONIZED GAS KINEMATICS

The radial velocity was estimated from the strongest emission lines present in the spectra, namely Hγ $\lambda 4340$, Hβ $\lambda 4861$, [O III] $\lambda 5007$, H α λ 6563, [N II] $\lambda 6584$ and [S II] $\lambda 6717$. The final radial

Table 1. Journal of observations.

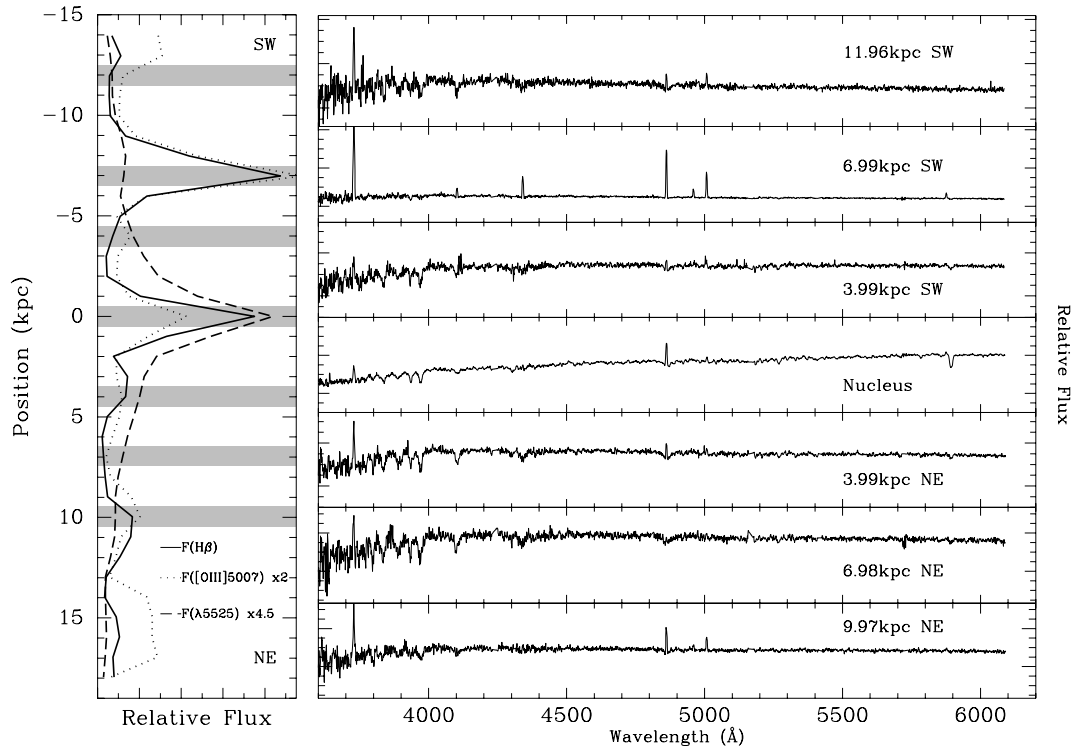| Date (UT)	Exposure time(s)	PA (°)	Δλ (Å)
2006 June 20	4 × 700	190	4280–7130
2006 June 20	4 × 700	238	4280–7130
2007 June 24	4 × 700	190	3350–6090
2007 June 24	4 × 700	238	3350–6090
2007 June 24	4 × 700	118	3350–6090

Figure 2. Spatial profiles of Hβ, [O III] $\lambda 5007$ and $\lambda 5525$ flux along PA = 238° for AM 2306A (left-hand side); and a sample spectra in the range of 3600–6000 Å from different regions along PA = 238° for AM 2306A as marked in the shaded areas in the spatial profiles (right-hand side). The spectra have been normalized at $\lambda 5870$ Å and are plotted in the rest-frame wavelength.
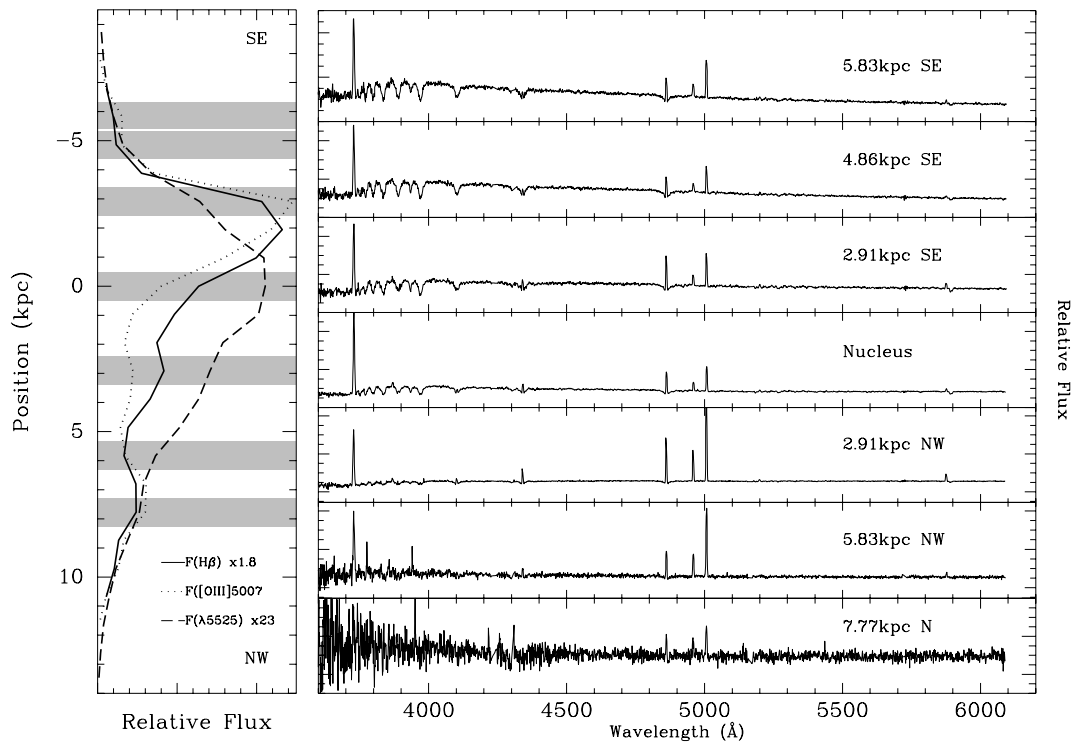

Figure 3. Same as Fig. 2, but along PA = 118° for AM 2306B.

velocity for each spectrum was obtained by averaging the individual measurements from the detected emission lines, and the errors estimated from the standard deviation of these measurements around that mean.

Using the acquisition images in the r' filter, we did a simple isophote fitting using the STSDAS.ELLIPSE task to obtain the position angle of the major and minor axes of both galaxies. We found that the major axis for AM 2306A is at PA = 236°, and for AM 2306B
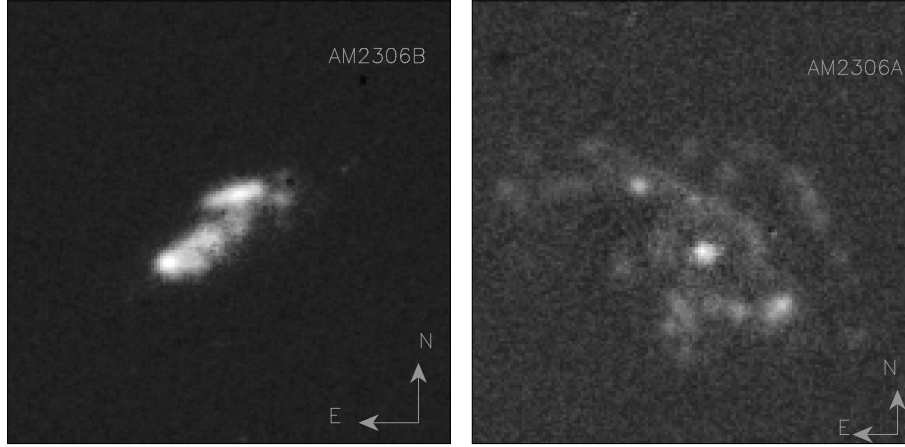
Figure 4. Hα image of AM 2306B (left-hand side) and AM 2306A (right-hand side). Description and detailed analysis of these images have been presented in FP04.
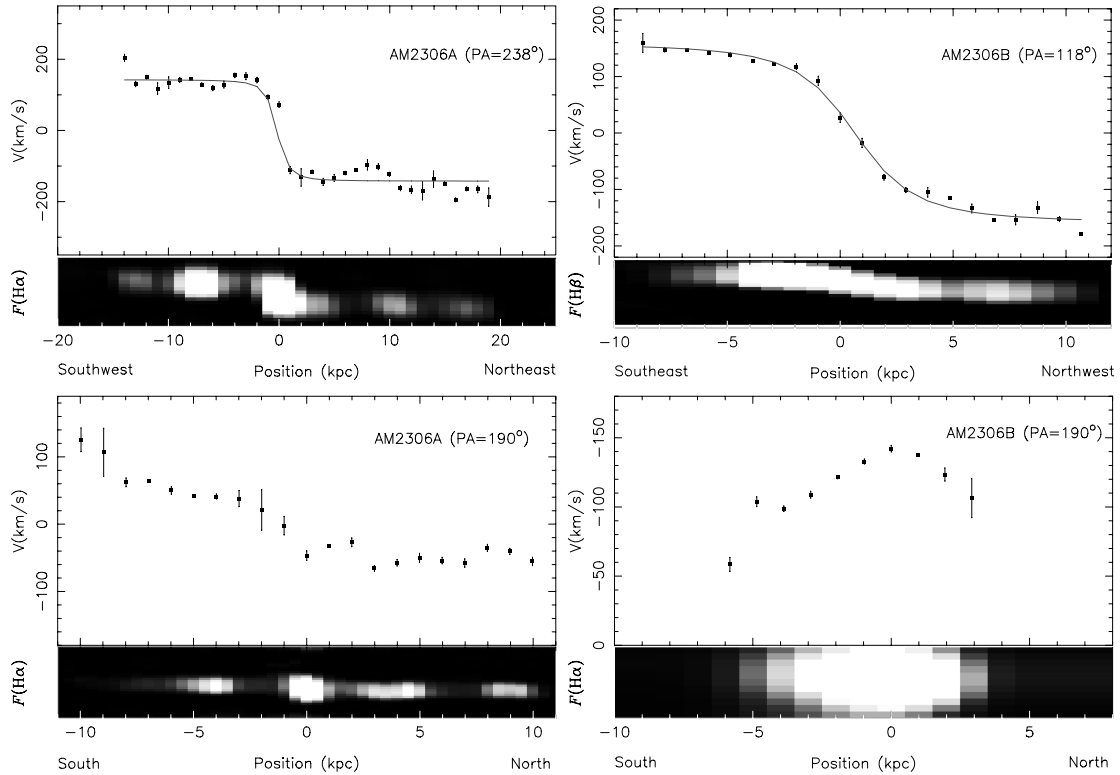

Figure 5. Observed mean radial velocity and two-dimensional spectra of Hα and Hβ emission lines as a function of apparent galactocentric distance. The left-hand panels show the kinematics along PA = 238° (top) and 190° (bottom) of AM 2306A, respectively. The right-hand panels show the kinematics along PA = 118° (top) and 190° (bottom) of AM 2306B, respectively. The velocity scale corresponds to the observed and model values after subtraction of the systemic velocity of each galaxy, without correction by the inclination in the plane of the sky.

at PA = 118°. The inclination of each galaxy with respect to the plane of the sky was also computed as cos $(i) = b/a$, where a and b are the minor and major semi-axes of the galaxy, respectively. We obtained $i = 56°$ for the main galaxy and $i = 60°$ for the secondary, in agreement with the values measured by FP04.

The rotation curves along the observed slit positions for both galaxies are presented in Fig. 5, as well as the corresponding two-dimensional spectra of Hα and/or Hβ emission lines. The radial velocity values after subtraction of the systemic velocities (as de-

termined from the rotation model described below) are listed in Table 2.

Both galaxies show a fairly symmetric rotation curve, so we adopted a very simple approximation for the observed velocity distribution, assuming that the gas moves under a logarithmic gravitational potential, following circular orbits close to a plane $P(i, \psi_0)$, characterized by its inclination to the plane of the sky *(i)* and the position angle (PA) of the line of nodes ψ_0. This assumption results in an observed radial circular velocity $v(r, \psi)$ in the plane of the

Table 2. Radial velocities. This is a sample of the full table that is available as Supporting Information.

AM 2306A				AM 2306B			
PA = 238°		PA = 190°		PA = 118°		PA = 190°	
R (kpc)	V (km s^{-1})	R (kpc)	V (km s^{-1})	R (kpc)	V (km s^{-1})	R (kpc)	V (km s^{-1})
13.96 SW	204 ± 10	13.96 S	. . .	. . .	. . .	. . .	. . .
12.96 SW	131 ± 8	12.96 S	. . .	. . .	. . .	. . .	. . .
11.96 SW	150 ± 5	11.96 S	. . .	. . .	. . .	. . .	. . .
10.97 SW	118 ± 16	10.97 S	. . .	. . .	. . .	. . .	. . .
9.97 SW	134 ± 16	9.97 S	125 ± 18	. . .	. . .	. . .	. . .

Table 3. Kinematical parameters.

	AM 2306A (PA = 238°)	AM 2306B (PA = 118°)
Parameter	Model	Model
V_s (km s^{-1})	8919 ± 5	8669 ± 3
V_0 (km s^{-1})	175 ± 6	185 ± 6
R_c (kpc)	1 ± 0.3	1.6 ± 0.2

sky given by Bertola et al. (1991):

$$v(r, \psi) = V_s + \frac{V_0 R \cos(\psi - \psi_0) \sin(i) \cos(i)}{\sqrt{R^2 \eta + R_c^2 \cos^2(i)}}, \quad (1)$$

with

$$\eta \equiv [\sin^2(\psi - \psi_0) + \cos^2(i) \cos^2(\psi - \psi_0)], \quad (2)$$

where V_s is the systemic velocity, R is the radius in the plane of the galaxy and V_0 and R_c are parameters that define the amplitude and shape of the curve. The fit of the rotation curves for each galaxy are shown in Fig. 5 and the parameters obtained are listed in Table 3.

The heliocentric velocity of the main galaxy is found to be 8919 km s^{-1}. The rotation curve obtained for AM 2306A along PA = 238° is well represented by the simple model above. This rotation curve is typical of spiral discs, rising shallowly and flattening at an observed amplitude of 145 km s^{-1}. As can be seen in Fig. 5, there are pronounced velocity features indicating local deviations from a smooth rotational field. One of such well-defined features is located towards the northeast along PA = 238°, at about 8 kpc projected distance from the nucleus, with an amplitude (peak to peak) of about 100 km s^{-1}. This feature is located where the slit crosses the outer spiral arm as seen in the Hα image (Fig. 4, right-hand side). This image also makes more obvious the disturbed spiral structure of the main component, very likely due to the interaction with AM 2306B.

For the secondary galaxy, the rotation curve model results in an heliocentric velocity of 8669 km s^{-1}. The observed radial velocities along PA = 118° are also very well represented by the model. The rotation curve is quite similar to that of AM 2306A, rising shallowly and flattening at an observed amplitude of about 158 km s^{-1}. Although the young star-forming population of the secondary galaxy show clear morphological irregularities (Fig. 4, left-hand side), the rotation curve does not present significant deviations from the smooth representation of the velocity field.

Donzelli & Pastoriza (1997) estimated systemic velocities of 8762 and 9069 km s^{-1} for AM 2306A and AM 2306B, respectively. Following our results, we verified that the values presented by those authors were reversed, and therefore our estimates are found to agree to within 2 per cent with those previous determinations.

An estimate of the dynamical mass can be derived by assuming that the mass inside a certain radius is given by $M(R) = RV^2/G$. For the main galaxy, the deprojected velocity amplitude is 175 km s^{-1} and its dynamical mass is 1.29×10^{11} M$_\odot$ within a radius of 18 kpc. For the companion galaxy, the deprojected velocity amplitude is 185 km s^{-1} and the dynamical mass within a radius of 10.7 kpc is $M(R) = 8.56 \times 10^{10}$ M$_\odot$. It is important to emphasize that the maximum radius to which we can observe the gas in emission is quite certainly smaller than the total radius of the galaxies, so our estimates of the dynamical mass give a lower limit to the actual dynamical mass of each system.

In determining the dynamical mass, the main source of error is in the estimation of the deprojected velocity, which in turn is highly dependent on the assumed inclination of the galaxies with respect to the plane of the sky. For AM 2306A, the inclination angle is well determined from the isophote fitting, with an estimated error of about 1 per cent, propagating to a 2 per cent uncertainty in the resulting total mass. For AM 2306B, the irregular morphology of the disc in optical images implies that the calculated value of the inclination angle varies significantly with radius. In this case, if we considered the isophote fitting from the regions more perturbed of AM 2306B to estimate the inclination angle, a maximum angle inclination of about 12 per cent would be obtained, implying in a reduction of up to 18 per cent in the total mass.

4 NUMERICAL SIMULATIONS

In order to reconstruct the history of the AM 2306-721 system and to predict the evolution of the encounter, we modelled the interaction between AM 2306A and AM 2306B through numerical simulations using the N-body/smoothed particle hydrodynamics code GADGET-2 developed by Springel (2005). The galaxies were modelled following the prescription of Hernquist (1993), including a gaseous disc component. The observed morphology and rotation curves presented in Section 3 provide the constraints to the simulations.

As for any study of this kind, recreating the evolution of the AM 2306-721 system requires solving the reverse problem of calculating the orbit followed by the two galaxies from their observed properties. This, like most similar cases, is not a fully determined problem, since the observations do not provide all the necessary information to uniquely identify the solution. Therefore, in order to restrict the parameter space when setting up the initial conditions for the simulations, we first calculate orbits that satisfy the constraint given by the observed radial velocity difference, testing different eccentricities, pericenter and line-of-sight direction distances. From that subset, based on the observed morphology, we select a few orbits to run the full simulations, from which the one that best fits the observed properties is selected.

The orbit that best reproduces the observational properties is found to be hyperbolic, with an eccentricity $e = 1.15$ and

Table 4. Parameters used on the simulations.

	AM 2306A	AM 2306B
Number of points in disc	2048	2048
Disc mass	0.5	0.17
Disc radial scalelength	0.6	0.6
Disc vertical scale thickness	0.06	0.05
Reference radius R_{ref}	0.06	1.2
Toomre Q at R_{ref}	1.5	1.5
Number of points in gas disc	2048	2048
Gas disc mass	0.05	0.017
Gas disc radial scalelength	1.0	0.75
Gas disc vertical scale thickness	0.02	0.03
Toomre Q at R_{ref}	1.5	1.5
Number of points in bulge	256	256
Bulge mass	0.08	0.01
Bulge radial scalelength	0.1	0.06
Number of points in spherical halo	2048	2048
Halo mass	3.5	1.7
Halo cutoff radius	8.0	4.0
Halo core radius	2.5	0.6

Notes: simulations were done in a system of units with $G = 1$. Model units scale to physical ones as: unit length is 3.5 kpc, unit velocity is 262 km s^{-1}, unit mass is 5.586×10^{10} M$_\odot$ and unit time is 13.062 Myr.

perigalacticum of $q = 5.25$ kpc . The orbital plane is perpendicular to the plane of the sky, and intersects the later in the line that connects AM 2306A and AM 2306B as projected in the sky. In perigalacticum, AM 2306B was behind AM 2306A, along the line of sight. The parameters for the best-fitting model are presented in Table 4. The composite rotation curve, as well as the individual model components and observed circular velocity, corrected by the inclination of each galaxy as given in Section 3, are shown in Fig. 6. The models indicate a total mass of 1.82×10^{11} M$_\odot$ for AM 2306A and of 8.68×10^{10} M$_\odot$ for AM 2306B. The mass of each individual component (disc, bulge, halo and gas) is quoted in Table 4.

Fig. 7 shows the time evolution of the encounter. Simulation starts 360 Myr before perigalacticum, and the time is shown in Myr in the upper right-hand corner of each frame. The situation that best reproduces the morphology and kinematics of AM 2306-721
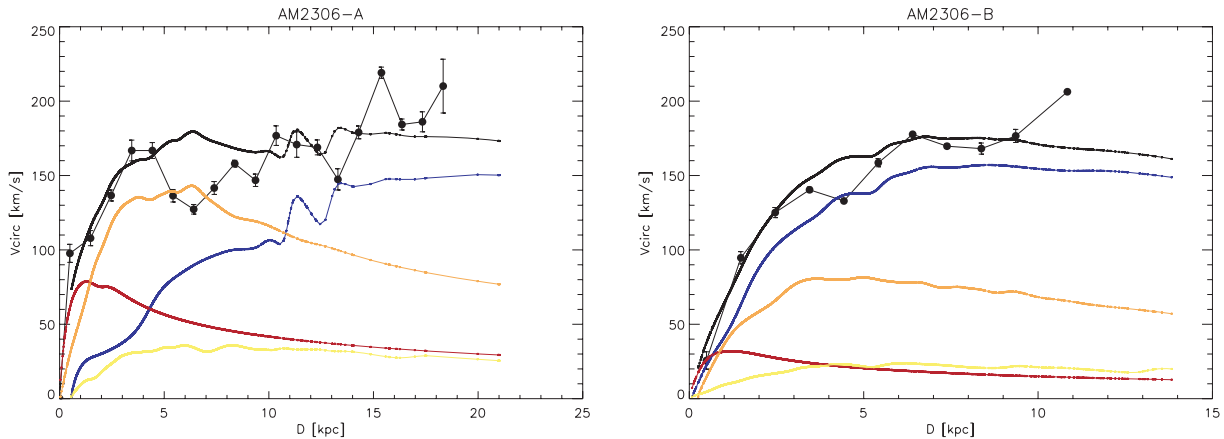
system at the current stage is $t = 610$ Myr or about 250 Myr after perigalacticum. The overall large-scale morphology and kinematics agree well with observations, considering the low resolution of the simulation.

5 STELLAR-POPULATION SYNTHESIS

A detailed study of the star formation in minor merger galaxies is an important source of information not only on the age distribution of their stellar-population components, but to better understand several aspects related to the interacting process, its effect in the properties of the individual galaxies and their later evolution. The absorption features arising from the stellar component also affect to different degrees the measured intensity of the emission line in the spectrum of the gaseous component. This effect is more prominent in, but not restricted to, the Balmer lines, so the stellar-population contribution must be subtracted from each spectra in order to investigate the physical properties of the gas in these galaxies.

To investigate the star-formation history of AM 2306A and AM 2306B, we use the stellar-population synthesis method developed by Bica (1998). This method employs the equivalent widths W_λ of several spectral absorption features and the measured continuum fluxes F_λ at different wavelengths, comparing them to those of a model computed from a base of simple stellar population (SSP) elements with known ages and metallicities. The algorithm generates all possible combinations of the base elements according to a given flux contribution step and compares the resulting W_λ and continuum points to the input ones. The allowed solutions are those which reproduce, within predefined limits, the observed W_λ and F_λ. All these possible solutions are then averaged, and this average is adopted as the final synthesis, with the uncertainty for each individual age component given by the standard deviation of the contribution from each allowed solution around the mean adopted value. The code used here is based on an upgraded version of the one presented by Schmitt, Bica & Pastoriza (1996), and includes a correction for the effect of the internal extinction.

The spectral windows for measuring W_λ are those defined in the Lick system (Worthey & Ottaviani 1997; Trager et al. 1998), with the addition of the K Ca II (corresponding to the spectral window $\lambda\lambda$ 3925–3945 Å) and H I λ3770 Å lines (spectral window $\lambda\lambda$3765–3785 Å). Previous to the measurements of the W_λ and F_λ, the

Figure 6. Circular velocity curves for galaxy models AM 2306A (left-hand side) and AM 2306B (right-hand side). The rotation curves of the individual model components are shown: halo in orange, bulge in red, stellar disc in blue and gas disc in yellow. The composite rotation curve is the continuous thick-black line. Points with error bars connected by thin black lines are the observed radial velocity curves, folded around the rotational centre and corrected by the inclination of each galaxy.
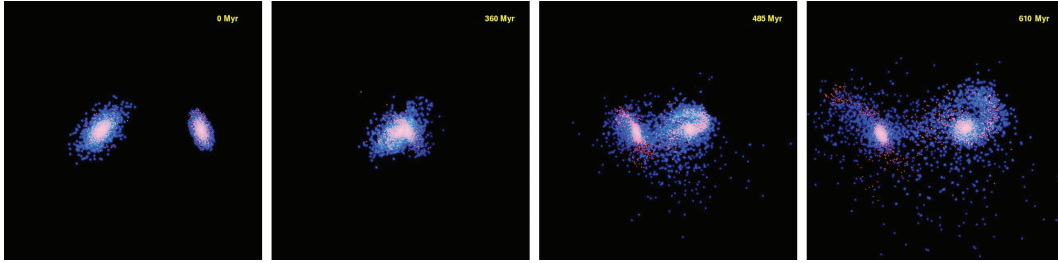
Figure 7. Four snapshots representing the evolution of the encounter. Time is shown in Myr in the upper right-hand corner of each frame, with respect to the beginning of the simulation. Stars are plotted in red, gas in blue. Orbital perigalacticum occurs at $t = 360$ Myr (upper right-hand frame). Best fit to current evolutionary stage of the AM 2306-721 system is about 250 Myr after perigalacticum (bottom right-hand frame).

Table 5. Equivalent widths of the absorption lines. This is a sample of the full table that is available as Supporting Information.

			Equivalent width (Å)			
R(kpc)	H I λ 3770	K Ca II	G λ 4300	Fe I λ 5270	Fe I λ 5709	Fe I λ 5782	NaD λ 5890
			AM 2306A (PA = 238°)			
3.99 SW	2.85 ± 0.40	. . .	. . .	. . .	. . .	0.69 ± 0.05	1.47 ± 0.01
2.99 SW	2.32 ± 0.19	5.46 ± 0.09	. . .	2.35 ± 0.03	. . .	0.60 ± 0.03	1.50 ± 0.01
1.99 SW	. . .	6.66 ± 0.07	3.80 ± 0.20	2.41 ± 0.07	. . .	0.61 ± 0.02	2.15 ± 0.02
1.00 SW	1.12 ± 0.12	5.69 ± 0.23	4.00 ± 0.31	2.15 ± 0.08	. . .	0.72 ± 0.04	3.31 ± 0.02
0	. . .	4.62 ± 0.09	3.10 ± 0.28	1.99 ± 0.01	. . .	0.75 ± 0.02	4.29 ± 0.02

spectra were corrected by the foreground (Galactic) reddening of $E(B - V) = 0.03$ mag taken from Schlegel, Finkbeiner & Davis (1998); and normalized to λ 5870 Å. The W_λ were measured using the *PACCE* code kindly provided by Vale et al. (in preparation). The W_λ values measured for each galaxy at different galactocentric distances and position angles are listed in Table 5.

The SSP base was created from the Bruzual & Charlot (2003) evolutionary stellar-population models, which are based on a high-resolution library of observed stellar spectra. This library allows us to derive detailed spectral evolution of SSPs across the wavelength range of 3200–9500 Å with a wide range of metallicities. We used the Padova 1994 tracks as recommended by Bruzual & Charlot (2003), with the initial mass function of Salpeter (Salpeter 1955). The final base contains five spectra corresponding to SSPs with ages of 2.5 Myr, 200 Myr, 1 Gyr, 5 Gyr and 10 Gyr, and solar metallicity. The adopted number of elements in the base was defined by a compromise between having enough age resolution, having a limited number of features available to constrain the fit, and the desire to maintain a consistent base for all apertures in both galaxies. For the few positions with higher S/N spectra in each galaxy, we tested a more detailed age grid, including components with ages 2.5 Myr, 100 Myr, 200 Myr, 500 Myr 1 Gyr, 5 Gyr and 10 Gyr, and solar metallicity. All those converged to the same results obtained with the original five-component base, with the contributions from the 100 and 500 Myr populations resulting always less than 5 per cent.

Fig. 8 shows an example of the observed spectra corrected for the reddening, the synthesized spectra and the pure emission spectra. Table 6 presents the result of the stellar-population synthesis for the individual spatial bins in each galaxy, stated as the percentual contribution of each base element to the flux at λ5870 Å. The values of $E(B - V)$ derived from the synthesis are also given in Table 6.

The spatial variations in the contributions of the stellar-population components are shown in Fig. 9. Large variations in the contribution from the different age components can be seen across the disc of both galaxies. The central regions of AM 2306A are dominated by the old (5–10 Gyr) population, with some significant contribution from a young 200 Myr and intermediate 1 Gyr component of the spiral arms and the disc. On the other hand, the stellar population in AM 2306B is overall much younger, being dominated by the 2.5 Myr, 200 Myr and 1 Gyr components, which are quite widely spread over the whole disc. The star-formation episode, occurred about 200 Myr ago in both galaxies, could be related with the perigalactic passage.

6 EMISSION LINE INTENSITIES AND O/H ABUNDANCE

Once the stellar-population contribution has been determined, the underlying absorption line spectrum can be subtracted to allow the correct measurement and analysis of the line emission from the gaseous component. The line intensities were measured using Gaussian line profile fitting on the pure emission spectra. We used the IRAF SPLOT routine to fit the lines, with the associated error being given as $\sigma^2 = \sigma_{cont}^2 + \sigma_{line}^2$, where σ_{cont} and σ_{line} are the continuum rms and the Poisson error of the line flux, respectively. The residual extinction associated with the gaseous component for each spatial bin was calculated comparing the observed Hγ/Hβ and Hα/Hβ ratios to the theoretical values in Hummer & Storey (1987) for an electron temperature of 10 000 K and a density of 100 cm^{-3}. The observed emission line intensities were then corrected by this residual extinction using the Howarth (1983) reddening function. Table 7 present the main emission line intensities normalized to the flux in the Hβ line. We derived the electron densities for AM 2306A from the [S II] λ 6717/λ 6731 intensity ratios, using the TEMDEN routine of the NEBULAR package from STSDAS/IRAF, assuming an electron temperature of 10 000 K. The energy levels, transition probabilities and collisional strength values for [S II] were taken,
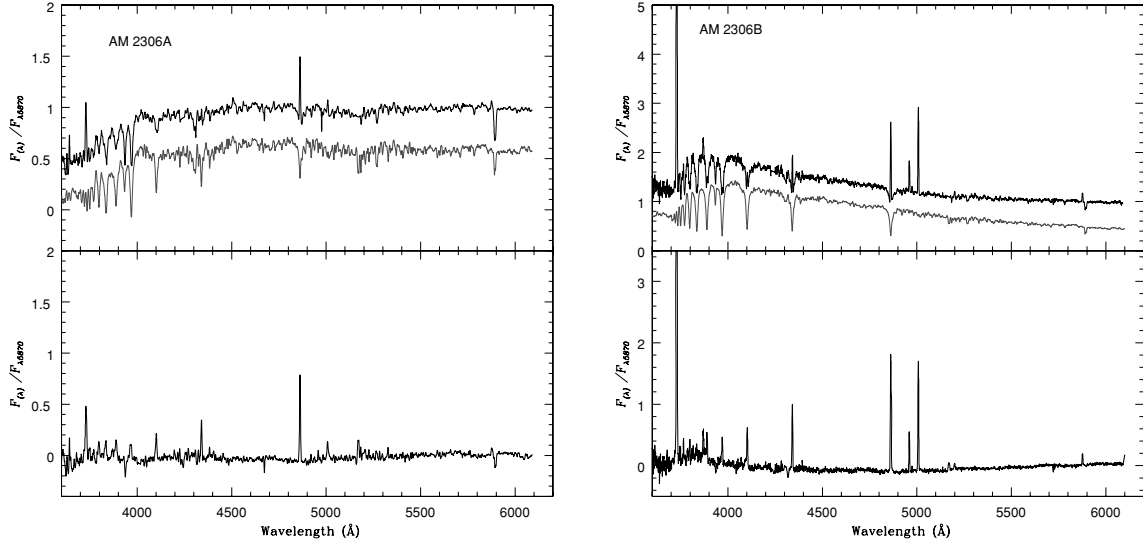
Figure 8. Stellar-population synthesis for central bin along the major axis of AM 2306A (left-hand side) and AM 2306B (right-hand side). Top panel: spectrum corrected for reddening and the synthesized spectrum (shifted by a constant). Bottom panel: pure emission spectrum.

Table 6. Stellar-population synthesis results.

R(kpc)	2.5 Myr	200 Myr	1 Gyr	5 Gyr	10 Gyr	$E(B-V)$
			Flux fraction at λ 5870 Å			
AM 2306-721A (PA = 238°)						
3.99 SW	15 ± 1	52 ± 2	3 ± 12	15 ± 62	15 ± 43	0.42 ± 0.21
2.99 SW	2 ± 1	14 ± 1	77 ± 9	1 ± 1	6 ± 10	0.16 ± 0.03
1.99 SW	2 ± 1	1 ± 1	76 ± 14	13 ± 42	8 ± 25	0.13 ± 0.02
1.00 SW	2 ± 1	8 ± 1	29 ± 4	16 ± 46	45 ± 28	0.18 ± 0.05
0	2 ± 1	22 ± 1	7 ± 9	13 ± 72	56 ± 47	0.29 ± 0.10
1.00 NE	1 ± 1	23 ± 3	1 ± 1	5 ± 27	70 ± 24	0.06 ± 0.01
1.99 NE	3 ± 1	1 ± 2	79 ± 8	12 ± 22	5 ± 13	0.14 ± 0.03
2.99 NE	3 ± 1	21 ± 2	75 ± 1	1 ± 1	0 ± 1	0.20 ± 0.05
3.99 NE	2 ± 1	24 ± 6	72 ± 9	1 ± 2	1 ± 1	0.07 ± 0.01
4.98 NE	0 ± 1	30 ± 1	49 ± 11	7 ± 19	14 ± 2	0.02 ± 0.01
5.98 NE	0 ± 1	39 ± 2	54 ± 18	4 ± 11	3 ± 7	0.13 ± 0.03
6.98 NE	0 ± 1	35 ± 6	63 ± 10	1 ± 2	1 ± 1	0.14 ± 0.03
7.98 NE	0 ± 1	50 ± 1	31 ± 10	9 ± 32	10 ± 27	0.22 ± 0.06
AM 2306-721B (PA = 118°)						
2.91 SE	32 ± 3	67 ± 6	1 ± 1	0 ± 0	0 ± 0	0.40 ± 0.46
1.94 SE	43 ± 3	55 ± 5	0 ± 1	1 ± 1	1 ± 1	0.35 ± 0.37
0.97 SE	22 ± 1	53 ± 2	11 ± 8	7 ± 18	7 ± 11	0.39 ± 0.18
0	16 ± 2	47 ± 4	13 ± 14	14 ± 54	10 ± 30	0.23 ± 0.07
0.97 NW	21 ± 1	45 ± 2	30 ± 6	2 ± 5	2 ± 3	0.39 ± 0.18
1.94 NW	20 ± 1	41 ± 2	36 ± 6	2 ± 5	1 ± 3	0.31 ± 0.12
2.91 NW	19 ± 1	42 ± 2	37 ± 3	1 ± 3	1 ± 2	0.28 ± 0.09
3.88 NW	15 ± 1	44 ± 2	36 ± 4	3 ± 4	2 ± 3	0.16 ± 0.04
4.86 NW	35 ± 1	63 ± 3	1 ± 1	1 ± 1	0 ± 1	0.31 ± 0.12
5.83 NW	19 ± 1	44 ± 1	34 ± 6	2 ± 5	1 ± 4	0.01 ± 0.01
6.80 NW	23 ± 1	25 ± 1	47 ± 20	3 ± 11	2 ± 4	0.02 ± 0.01
7.77 NW	16 ± 1	46 ± 2	36 ± 5	1 ± 4	1 ± 2	0.01 ± 0.01

respectively, from Bowen (1960), Keenan et al. (1993) and Ramsbottom, Bell & Stafford (1996). The resulting electron density obtained for AM 2306A is in the low-density limit for the [S II] lines, with values below $N_e = 630\,\mathrm{cm}^{-3}$, compatible with the results for both galactic (Copetti et al. 2000), and giant extragalactic H II regions (Castaneda, Vilchez & Copetti 1992).

The spatial metallicity variations across the disc of spiral galaxies are a fundamental parameter for understanding galaxy evolution. In isolated spiral galaxies, it is often found that the metallicity in the ionized interstellar medium decreases outwards (Vila-Costas & Edmunds 1992), while a weaker or absent metallicity gradient in interacting galaxies of similar morphological type have been pointed out as evidence of radial gas inflows driven by tidal torques generated during the interaction (Roy & Walsh 1997; Henry & Worthey 1999).

Determining accurate element abundances from optical spectra is critically dependent on measuring temperature sensitive line ratios, such as [O III] (λ 4959 + λ 5007)/λ 4363. However, when doing spectroscopy of H II regions with high metallicity and/or low excitation, temperature sensitive lines such as [O III] λ 4363 are found to be weak or unobservable, and empirical indicators based on more easily measured line ratios have to be used to estimate metal abundances. The line ratio R_{23} = ([O II] λ 3727 + [O III] λ 4959 + [O III] λ 5007)/Hβ, introduced by Pagel et al. (1979) has been widely used for determination of oxygen abundance in H II regions (Vila-Costas & Edmunds 1992; Zaritsky, Kennicutt & Huchra 1994; Gil de Paz et al. 2007).

Although the R_{23} indicator is sensitive to abundance variations, it is double valued, presenting high- to low- metallicity turnover in the range of $8 < 12 + \log(O/H) < 8.3$ (Pilyugin & Thuan 2005). Another critical issue regarding the use of the R_{23} is the fact that it is also sensitive to the ionization level of the emission gas, especially at low metallicities. These problems can be solved, by choosing either the low- or high-metallicity branch of R_{23}, and combining it with another line indicator sensitive to the ionization level, such as the ratio [O II] (λ 3727 + λ 3729)/[O III] λ 5007 (McGaugh 1991).

Since we do not detect any temperature-sensitive emission lines in our spectra, we used the R_{23} indicator to estimate the metallicity comparing the observed values with a grid of photoionization models obtained from the code CLOUDY/96.03 (Ferland 2002). The grid was built following the same procedures as Dors & Copetti (2006), with metallicities of Z = 2.0, 1.1, 1.0, 0.6 and 0.4 $Z_\odot$, and ionization parameter $\log U = -2, -2.5$ and -3. The solar value of $12 + \log(O/H) = 8.69$ is taken from Allende Prieto, Lambert & Asplund (2001). For each model, the ionizing source was assumed

Table 7. Dereddened line fluxes $I(\lambda)$. This is a sample of the full table that is available as Supporting Information.

						AM 2306A (PA = 238°)					
R (kpc)	c(Hβ)	[O II] λ3727	H I λ4340	H I λ4861	[O III] λ4949	[O III] λ5007	[N II] λ6548	H I λ6562	[N II] λ6584	[S II] λ6717	[S II] λ6731
12.96 SW	0	...	...	100 ± 3	40 ± 2	118 ± 4	22 ± 4	286 ± 19	60 ± 5	73 ± 10	73 ± 10
11.96 SW	0.10	...	47 ± 9	100 ± 4	...	72 ± 4	29 ± 7	286 ± 25	94 ± 10	94 ± 14	86 ± 14
10.97 SW	0	...	...	100 ± 5	...	62 ± 4	54 ± 13	286 ± 33	117 ± 17	...	...
9.97 SW	0	...	...	100 ± 4	...	55 ± 3	...	286 ± 27	121 ± 15	...	...
8.97 SW	0	...	...	100 ± 3	...	61 ± 3	34 ± 5	286 ± 18	101 ± 8	89 ± 4	65 ± 4

Notes: all fluxes normalized to $F(H\beta)$ as listed in Column 5.
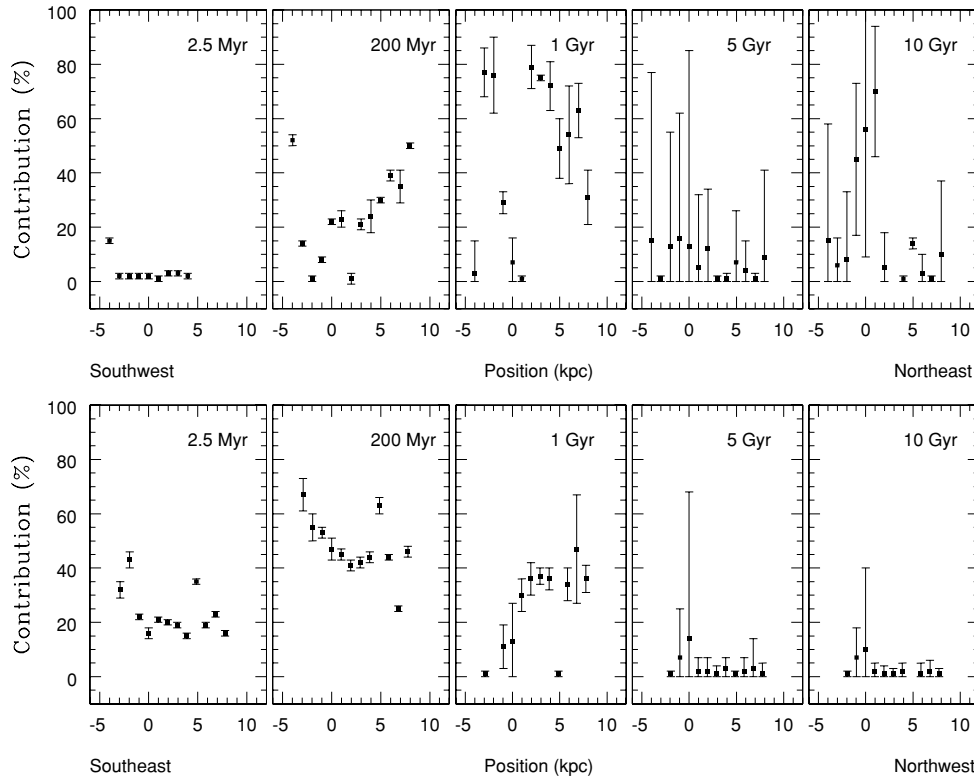
Figure 9. Synthesis results in flux fractions as a function of distance to the centre along the major axis of AM 2306A (upper panel) and AM 2306B (bottom panel).

to be a stellar cluster with energy distribution obtained using the stellar-population synthesis code *STARBURST* 99 (Leitherer et al. 1999), with an upper mass limit of $100\,M_\odot$ and an age of 2.5 Myr. Fig. 10 shows the R_{23} versus [O II]/[O III] diagramme, with the observed values superposed in the computed models. Open squares correspond to regions in AM 2306A, filled triangles to regions in AM 2306B. Most of the points indicate gas with solar or less than solar abundance, with the exception of two spatial bins in AM 2306A, corresponding to the nuclear and the 1.0 kpc north east regions. Figs 11 and 12 show the estimated O/H abundance distribution as a function of the galactocentric distance, R_G, for AM 2306A and AM 2306B, respectively.

The disc of the main galaxy (Fig. 11) shows a clear radial oxygen abundance gradient, that can be fitted as a linear function $12 + \log(O/H) = 8.75(\pm 0.06) - 0.025(\pm 0.007)\,R_G$, where R_G is in kpc. This abundance gradient is typical of spiral galaxies, as found in M 101 (Kinkel & Rosa 1994; Garnett et al. 1999), and in NGC 1365 (Pilyugin, Contini & Vílchez 2004; Dors & Copetti 2005). For AM 2306B, the oxygen abundance is relatively homogeneous across the galaxy disc, not presenting a radial-oxygen abundance gradient.

The observed values are in the range $8.30 < 12 + \log(O/H) < 8.58$.

The above results are in agreement with the luminosity-metallicity relation for gas rich galaxies (e.g. Zaritsky et al. 1994; Contini et al. 2002; Lamareille et al. 2004; Tremonti et al. 2004), in the sense that more luminous objects are more metallic. To investigate if the interaction affected the gas metallicity in both galaxies, we compare the central O/H value of AM 2306A and AM 2306B with isolated and pair galaxies from the sample of Kewley et al. (2006). We found the central O/H value for AM 2306A is in agreement with the results obtained by Kewley et al. (2006) for field galaxies at same luminosity, indicating that the interaction has not significantly affected the gas abundance in AM 2306A. On the other hand, the central O/H value obtained for AM 2306B is about 0.1–0.2 dex lower than those estimated by Kewley et al. (2006) for field galaxies at same luminosity, but is in good agreement with the values obtained for galaxies in pairs.

Interestingly, the mean value for AM 2306B, $12 + \log(O/H) = 8.39$, is similar to the values found in the outer parts of AM 2306A. If we assume that in AM 2306B there was an oxygen abundance
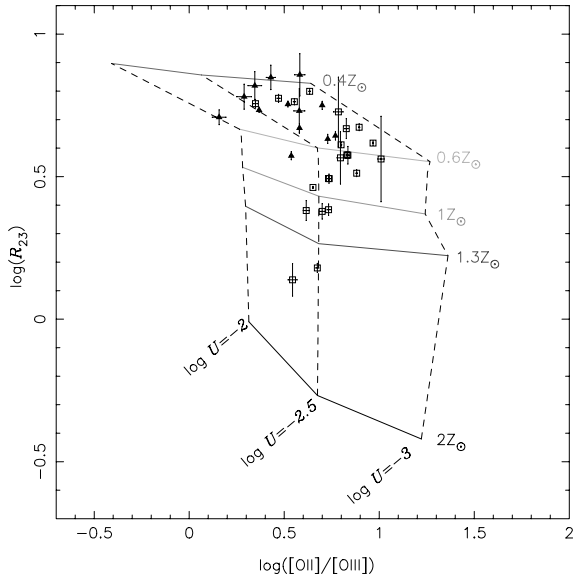
Figure 10. The relation $\log(R_{23})$ versus $\log([O\,\textsc{ii}]/[O\,\textsc{iii}])$ for the individual spatial bins in AM 2306A (squares) and AM 2306B (triangles). The curves represent the photoionization models described in the text (dashed lines correspond to different values of the ionization parameter, solid lines to different gas metallicity).
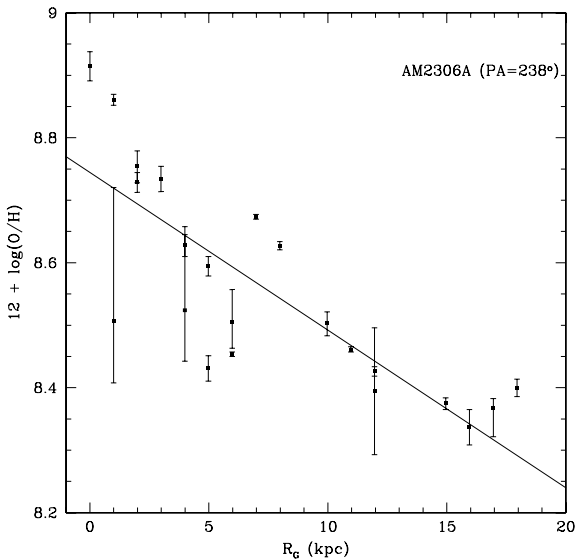

Figure 11. The O/H abundance distribution as a function of galactocentric radius for the main galaxy along of the major axis. The solid line represents the fit of the data.

gradient before the encounter with AM 2306A, and that this gradient was destroyed by gas flows from the outer parts to the centre of the galaxy, mixing and homogenizing the chemical composition of the interstellar medium (Kewley et al. 2006), we can estimate the fraction of infalling gas that was required to produce the metallicities that are now observed in AM 2306B. For this, we assume that, before the interaction, AM 2306B presented the same O/H gradient observed now in AM 2306A. To reduce the initial abundance of $12 + \log(O/H) \sim 8.75$ in the central region to the current mean value of 8.39, it would be necessary that the central gas was diluted so as to contain a fraction of 56 per cent of poor gas from the outer
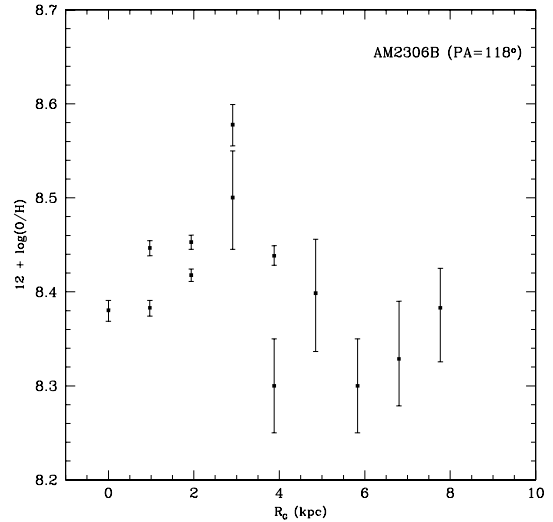

Figure 12. The O/H abundance distribution as a function of galactocentric radius for the secondary galaxy along of the major axis.

disc plus 44 per cent of rich gas from the central region of the galaxy.

Another possible explanation to mix the interstellar medium and flatten the radial gradient would be the presence of a bar Friedli, Benz & Kennicutt (1994). However, the very disturbed luminosity profile of this galaxy in *B, V* and *I* images (FP04) do not show any evidence of such feature.

We can estimate the amount of ionized gas associated with the central star-forming complex in AM 2306 from the Hα luminosity of this region as given by Testor (2001). For $R_G < 0.2$ kpc, we have $L(H\alpha) = 2.71 \times 10^{41}$ erg s^{-1} (FP04), and assuming a filling factor of $f = 0.30$, we find a mass of ionized gas of $M_{H\,\textsc{i}} = 8.3 \times 10^5$ M$_\odot$. According to the above-proposed scenario, 56 per cent of this total mass (4.6×10^5 M$_\odot$) would be infalling gas from the outer parts of the galaxy. Since we do not see any evidence of ionized gas flows in the radial velocities, we have to assume that the process of gas infall has already stopped. Considering the result of the numerical simulations, we take a time-scale of ~ 100 Myr for the infall process (the gas motions were triggered by the perigalactic passage 250 Myr ago, but are no longer observable), resulting in an infall rate of 0.01 M$_\odot$ yr^{-1}. This infall rate is considerably smaller than the average gas inflow rate of 7 M$_\odot$ yr^{-1} to the central 1–2 kpc predicted by recent merger models (Iono, Yun & Mihos 2004).

7 CONCLUSIONS

An observational study about the effects of the interactions in the kinematics, stellar population and abundances of the galaxy pair AM 2306-721 is performed. The data consist of long-slit spectra in the wavelength range of 3350–7130 Å obtained with the Gemini Multi-Object Spectrograph at Gemini South. The main findings are the following.

(i) Rotation curves of the main and companion galaxies with an deprojected velocity amplitude of 175 and 185 km s^{-1}, respectively, were obtained. An estimate of the dynamical mass was derived for each galaxy, using the deprojected velocity amplitude. For the main galaxy, its dynamical mass is 1.29×10^{11} M$_\odot$ within a radius of 18 kpc; and for the companion galaxy, the estimated dynamical mass is $M(R) = 8.56 \times 10^{10}$ M$_\odot$ within a radius of 10.7 kpc.

(ii) In the main galaxy, radial-velocity deviations from the disc rotation of about 100 km s^{-1} were detected, which are probably due to the interaction with the companion galaxy.

(iii) In order to reconstruct the history of the AM 2306-721 system and to predict the evolution of the encounter, we modelled the interaction between AM 2306A and AM 2306B through numerical *N*-body/hydrodynamical simulations. The orbit that best reproduces the observational properties is found to be hyperbolic, with an eccentricity $e = 1.15$ and perigalacticum of $q = 5.25$ kpc; the current stage of the system would be about 250 Myr after perigalacticum.

(iv) The spatial variations of the stellar-population components of the galaxies were analysed by fitting combinations of stellar-population models of different ages (2.5 Myr, 200 Myr, 1 Gyr, 5 Gyr and 10 Gyr) and solar metallicity. The central regions of the main galaxy are dominated by the old (5–10 Gyr) population, with some significant contribution from a young 200 Myr and intermediate 1 Gyr component along the disc of the galaxy. On the other hand, the stellar population in the companion galaxy is overall much younger, being dominated by the 2.5 Myr, 200 Myr and 1 Gyr components, which are quite widely spread over the whole disc.

(v) Oxygen abundance spatial profiles were obtained using a grid of photoionization models and the $R_{23} = ([\text{O\,\textsc{ii}}]\,\lambda\,3727 + [\text{O\,\textsc{iii}}]\,\lambda\,4959 + [\text{O\,\textsc{iii}}]\,\lambda\,5007)/\text{H}\beta$ line ratio. The disc of the main galaxy shows a clear radial oxygen abundance gradient, that can be fitted as a linear function $12 + \log(\text{O/H}) = 8.75(\pm 0.06) - 0.025(\pm 0.007)R_G$; in the companion galaxy the oxygen abundance is relatively homogeneous across the galaxy disc, with the observed mean value of $12 + \log(\text{O/H}) = 8.39$.

(vi) The absence of an abundance gradient in the secondary galaxy is interpreted as it is having been destroyed by gas flows from the outer parts to the centre of the galaxy.

ACKNOWLEDGMENTS

REFERENCES

Allende Prieto C., Lambert D. L., Asplund M., 2001, ApJ, 556, L63
Arp H. C., Madore B. F., 1987, by Halton C. Arp and Barry F. Madore, A Catalogue of Southern Peculiar Galaxies and Associations. Cambridge Univ. Press, Cambridge, p. 504
Barnes J. E., Hernquist L., 1996, ApJ, 471, 115
Barton E. J., Geller M. J., Kenyon S. J., 2000, ApJ, 530, 660
Barton Gillespie E., Geller M. J., Kenyon S. J., 2003, ApJ, 582, 668
Bertola F., Bettoni D., Danziger J., Sadler E., Sparke L., de Zeeuw T., 1991, ApJ, 373, 369
Bica E., 1988, A&A, 195, 9
Bushouse H. A., 1986, AJ, 91, 255
Bowen I. S., 1960, ApJ, 132, 1
Bruzual G., Charlot S., 2003, MNRAS, 344, 1000

Castaneda H. O., Vilchez J. M., Copetti M. V. F., 1992, A&A, 260, 370
Contini T., Treyer M. A., Sullivan M., Ellis R. S., 2002, MNRAS, 330, 75
Copetti M. V. F., Mallmann J. A. H., Schmidt A. A., Castañeda H. O., 2000, A&A, 357, 621
Dalcanton J. J., 2007, ApJ, 658, 941
Donzelli C. J., Pastoriza M. G., 1997, ApJ, 111, 181
Dors O. L., Jr, Copetti M. V. F., 2005, A&A, 437, 837
Dors O. L., Jr, Copetti M. V. F., 2006, A&A, 452, 473
Dutil Y., Roy J.-R., 1999, ApJ, 516, 62
Ellison S. L., Patton D. R., Simard L., McConnachie A. W., 2008, AJ, 135, 1877
Ferland G. J., 2002, Hazy, A Brief Introduction to Cloudy 96.03, Univ. Kentucky, Dept. Phys., Astron. internal report
Ferreiro D. L., Pastoriza M. G., 2004, A&A, 428, 837 (FP04)
Ferreiro D. L., Pastoriza M. G., Rickes M., 2008, A&A, 481, 645
Friedli D., Benz W., Kennicutt R., 1994, ApJ, 430, L105
Garnett D. R., Shields G. A., Peimbert M., Torres-Peimbert S., Skillman E. D., Dufour R. J., Terlevich E., Terlevich R. J., 1999, ApJ, 513, 168
Geller M. J., Kenyon S. J., Barton E. J., Jarrett T. H., Kewley L. J., 2006, AJ, 132, 2243
Gil de Paz A. et al., 2007, ApJ, 661, 115
Keenan F. P., Hibbert A., Ojha P. C., Conlon E. S., 1993, Phys. Scr., 48, 129
Kennicutt R. C., Jr, Keel W. C., 1984, ApJ, 279, L5
Kennicutt R. C., Jr, Roettiger K. A., Keel W. C., van der Hulst J. M., Hummel E., 1987, AJ, 93, 1011
Kewley L. J., Geller M. J., Barton E. J., 2006, AJ, 131, 2004
Koeppen J., Arimoto N., 1990, A&A, 240, 22
Henry R. B. C., Worthey G., 1999, PASP, 111, 919
Hernquist L., 1993, ApJ, 86, 389
Hernquist L., Mihos J. C., 1995, ApJ, 448, 41
Howarth I. D., 1983, MNRAS, 203, 301
Hummel E., 1981, A&A, 96, 111
Hummer D. G., Storey P. J., 1987, MNRAS, 224, 801
Iono D., Yun M. S., Mihos J. C., 2004, ApJ, 616, 199
Joseph R. D., Wright G. S., 1985, MNRAS, 214, 87
Lamareille F., Mouhcine M., Contini T., Lewis I., Maddox S., 2004, MNRAS, 350, 396
Lambas D. G., Tissera P. B., Alonso M. S., Coldwell G., 2003, MNRAS, 346, 1189
Larson R. B., Tinsley B. M., 1978, ApJ, 219, 46
Leitherer C. et al., 1999, ApJ, 123, 3
Kinkel U., Rosa M. R., 1994, A&A, 282, L37
Kronberger T., Kapferer W., Schindler S., Böhm A., Kutdemir E., Ziegler B. L., 2006, A&A, 458, 69
McGaugh S. S., 1991, ApJ, 380, 140
Mihos J. C., Hernquist L., 1996, ApJ, 464, 641
Nikolic B., Cullen H., Alexander P., 2004, MNRAS, 355, 874
Noguchi M., 1988, A&A, 203, 259
Pagel B. E. J., Edmunds M. G., Blackwell D. E., Chun M. S., Smith G., 1979, MNRAS, 189, 95
Pilyugin L. S., Thuan T. X., 2005, ApJ, 631, 231
Pilyugin L. S., Contini T., Vílchez J. M., 2004, A&A, 423, 427
Ramsbottom C. A., Bell K. L., Stafford R. P., 1996, Atomic Data and Nuclear Data Tables, 63, 57
Roy J.-R., Walsh J. R., 1997, MNRAS, 288, 715
Rubin V. C., Waterman A. H., Kenney J. D. P., 1999, AJ, 118, 236
Salpeter E. E., 1955, ApJ, 121, 161
Schmitt H. R., Bica E., Pastoriza M. G., 1996, MNRAS, 278, 965
Schlegel D. J., Finkbeiner D. P., Davis M., 1998, ApJ, 500, 525
Sekiguchi K., Wolstencroft R. D., 1992, MNRAS, 255, 581
Springel V., 2005, MNRAS, 364, 1105
Struck C., 1999, Phys. Rep., 321, 1
Testor G., 2001, A&A, 372, 667
Trager S. C., Worthey G., Faber S. M., Burstein D., Gonzalez J. J., 1998, ApJ, 116, 1
Tremonti C. A. et al., 2004, ApJ, 613, 898
Vila-Costas M. B., Edmunds M. G., 1992, MNRAS, 259, 121
Woods D. F., Geller M. J., 2007, AJ, 134, 527

Worthey G., Ottaviani D. L., 1997, ApJ, 111, 377
Zaritsky D., Kennicutt R. C., Jr, Huchra J. P., 1994, ApJ, 420, 87

SUPPORTING INFORMATION

Additional Supporting Information may be found in the online version of this article.

Please note: Blackwell Publishing are not responsible for the content or functionality of any supporting information supplied by the authors. Any queries (other than missing material) should be directed to the corresponding author for the article.

This paper has been typeset from a TEX/LATEX file prepared by the author.